

RESEARCH ARTICLE

Effect of network connectivity on behavior of synthetic Broborg hillfort glasses

José Marcial^{1,2}  | Maria Rita Cicconi³ | Carolyn I. Pearce¹ | Jaroslav Kloužek^{2,4} | James J. Neeway¹ | Richard Pokorný^{2,4}  | Miroslava Vernerová^{2,4} | John S. McCloy⁵  | Emily T. Nienhuis¹ | Rolf Sjöblom⁶ | Jamie L. Weaver⁷  | Russell J. Hand⁸  | Pavel Hrma⁹ | Daniel R. Neuville⁴  | Albert A. Kruger¹⁰ 

¹Pacific, Northwest National Laboratory, Richland, Washington, USA

²University of Chemistry and Technology Prague, Prague, Czechia

³Institut de Physique du Globe de Paris, CNRS, Géomatériaux, Université de Paris, Paris, France

⁴Institute of Rock Structure and Mechanics of the Czech Academy of Sciences, Prague, Czechia

⁵School of Mechanical and Materials Engineering, Washington State University, Pullman, Washington, USA

⁶Tekedo AB., Nyköping, Sweden

⁷Material Measurement Laboratory, National Institute of Standards and Technology, Gaithersburg, Maryland, USA

⁸Department of Materials Science and Engineering, University of Sheffield, Sheffield, UK

⁹AttainX, Support Services Contractor to The Office of River Protection, U.S. Department of Energy, Richland, Washington, USA

¹⁰U.S. Department of Energy, Office of River Protection, Richland, Washington, USA

Correspondence

José Marcial, Pacific Northwest National Laboratory, Richland, WA 99352, USA.
Email: Jose.Marcial@pnl.gov

Present address

Maria Rita Cicconi, Friedrich-Alexander-Universität Erlangen-Nürnberg, Institute of Glass and Ceramics, Martensstr. 5, 91058 Erlangen, Germany.

Funding information

Czech Ministry of Education, Youth and Sports, Grant/Award Number: LTAUSA18075; U.S. Department of Energy (DOE) Waste Treatment and Immobilization Plant Project, Grant/Award Number: DE-sAC05-76RL01830

Abstract

There is wide industrial interest in developing robust models of long-term (>100 years) glass durability. Archeological glass analogs, glasses of similar composition, and alteration conditions to those being tested for durability can be used to evaluate and inform such models. Two such analog glasses from a 1500-year-old vitrified hillfort near Uppsala, Sweden have previously been identified as potential analogs for low concentration Fe-bearing aluminosilicate nuclear waste glasses. However, open questions remain regarding the melting environment from which these historic glasses were formed and the effect of these conditions on their chemical durability. A key factor to answering the previous melting and durability questions is the redox state of Fe in the starting and final materials. Past work has shown that the melting conditions of a glass-forming melt may influence the redox ratio value ($\text{Fe}^{+3}/\sum\text{Fe}$), a measure of a glass's redox state, and both melting conditions and the redox ratio may influence the glass alteration behavior. Synthetic analogs of the hillfort glasses have been produced using either fully oxidized or reduced Fe precursors to address this question.

This is an open access article under the terms of the [Creative Commons Attribution](https://creativecommons.org/licenses/by/4.0/) License, which permits use, distribution and reproduction in any medium, provided the original work is properly cited.

© 2022 Battelle Memorial Institute and The Authors. *Journal of the American Ceramic Society* published by Wiley Periodicals LLC on behalf of American Ceramic Society. This article has been contributed to by U.S. Government employees and their work is in the public domain in the USA.

In this study, the melting behavior, glass transition temperature, oxidation state, network structure, and chemical durability of these synthesized glass analogs is presented. Resulting data suggests that the degree of network connectivity as impacted by the oxidation state of iron impacted the behavior of the glass-forming melt but in this case does not affect the chemical durability of the final glass. Glasses with a lower degree of melt connectivity were found to have a lower viscosity, resulting in a lower glass transition temperature and softening temperature, as well as in a lower temperature of foam onset and temperature of foam maximum. This lower degree of network connectivity most likely played a more significant role in accelerating the conversion of batch chemicals into glass than the presence of water vapor in the furnace's atmosphere. Future work will focus on using the results from this work with outcomes from other aspects of this project to evaluate long-term glass alteration models.

KEYWORDS

aluminosilicate glasses, cultural heritage materials, Fe, glass durability, glass redox

1 | INTRODUCTION

Predicting the chemical durability of nuclear waste glasses in a permanent geological or near-surface repository presents a significant experimental challenge. Natural and archaeological glass analogs allow the study of glass alteration over such timescales, albeit with no control over the sample alteration environment(s).^{1,2} An analog example can be found in the glasses from the Broborg hillfort site, located near Uppsala, Sweden. These glasses may be used to inform laboratory developed long-term glass alteration models and help define the long-term durability of select types of vitrified nuclear waste.^{1,3} However, small glass amounts were excavated from Broborg (<1 g) and do not enable direct alteration studies.⁴ As a result, new glasses based on the chemistries of the Broborg glasses need to be made and altered following established procedures. A key factor in synthesizing new materials is imitating the conditions under which the original solids were vitrified. How these new glasses are formed is important as (i) the reducing atmosphere and water vapor from the charcoal fire may have influenced the melting behavior of the raw materials and enhanced rock fusion using iron-age technology, and (ii) the oxidation state of the melt can influence the oxidation state of the final glass and, by extension, its chemical durability. These two questions are addressed in this paper.

Iron (Fe) is the most abundant polyvalent metal species in the Broborg samples and is an important component to glass melting and alteration processes. The oxidation state of Fe can affect atmospheric oxygen partial pressure, temperature, viscosity, and batch composition during glass melting.^{5–12} Its influence over these processes is due to how the oxidation state and coordination number of

Fe influence glass network connectivity through changing the number of non-bridging oxygen (NBO) atoms within the framework of the glass/melt.^{13,14} For example, the oxidation state of Fe has been previously correlated with melt viscosity.⁶ Decreased viscosity was observed to be caused by depolymerization (e.g., more NBOs) of the melt as a function of Fe reduction.⁶ A reducing atmosphere likely affected the viscosity of the low-Fe, high-silica felsic glass observed at Broborg given this outlined relationship between Fe oxidation state and viscosity along with the other previously listed processes.¹⁵

A depolymerized network resulting from the presence of Fe(II) in the glass can also increase the release rate of glass species in an aqueous environment during glass alteration.¹⁶ The oxidation state of Fe has the potential to affect the dissolution rate of the glass. At short time periods, if the iron is reduced and acting as a glass modifier, then this may affect the susceptibility of the glass to the ion exchange process. On the other hand, if the reduced iron is in a modifying role coupled with the fact that Fe(II) is more soluble than Fe(III), at longer time periods a more porous alteration layer may exist as the Fe(II) has leached into solution. This conceptual mechanism of glass alteration may lead to a less durable glass. Though studies exist on the role of iron concentration and oxidation state in solution,^{17–22} fewer studies assess the role of iron redox in the initial complex silicate glass. In the present study, the aim is not to explore these mechanisms, per se, but rather to assess the durability of the glasses with different iron redox states to determine whether or not their relative durability would differ.

Therefore, a reducing melt atmosphere may influence the glass's chemical durability. In Broborg samples, the

extent of this influence may vary depending on the relative fraction of the Fe-containing phases in the parent rocks. Specifically, the amphibolite has significantly less quartz (SiO_2) content, and more Fe than granite.^{4,23} The oxidation state of Fe in the synthetic glass thus needs to be like that of its archeological counterpart to run tractable glass alteration experiments.

It must also be stated that the chemical durability of glasses is not only a function of glass composition but is also by environmental parameters, such as site hydrology, solution pH, and solution composition.^{24–29}

To study the relative durability of the glasses with different iron redox chemistries, glass powders were altered using a 90°C static alteration test for up to 100 days. This method was previously used to alter samples from the Broborg hillfort and compare the alteration features to excavated samples.³⁰

A baseline redox state was determined for archeological and synthesized glasses using X-ray absorption near edge structure (XANES) analyses, high-temperature XANES, wet chemical methods, and high-temperature oxygen probe measurements. Melting behaviors of the synthetic glass were further investigated with dilatometry, evolved gas analysis (EGA), and volumetric batch expansion (VBE) measurements. EGA and VBE results will also provide insight into the effect of water on the materials' melting behaviors.^{31,32} It is suspected that water vapor was present in the melt atmosphere produced by the charcoal fires of Broborg; possibly lowering the melt viscosity and sealing the melting material with grass turf, and dehydrating hydrous amphiboles.¹⁵ Electron probe microanalysis (EPMA) results were used to test chemical comparability between the archeological and synthesized glasses. The relative alteration behavior of the oxide-state matched synthetic glass was examined with 100-day static alteration testing of quenched glass powders at 90°C.

2 | MATERIALS AND METHODS

2.1 | Sample preparation

An edifice was constructed ca. 1500 years ago at the Broborg site^{33–35} by heating quarried and surface collected rocks with stoked fires that were fueled either with wood and/or charcoal. This produced a vitrified matrix that fused sections of the inner rampart. Two vitreous materials are prevalent within the matrix of the Broborg site. The first material has been identified as felsic-like and is rich in quartz, plagioclase, and minor microcline, with higher and lower microcline content resulting in a red and a white granite, respectively.^{4,15,36} The second material is mafic-like and is an amphibolite comprising amphibole and

clinochlore with minor amounts of quartz, plagioclase, microcline, and mica.^{4,15,36}

The Broborg archeological glasses are as heterogeneous as their starting materials. They feature partially dissolved or recrystallized phases and multiple glassy phases.²³ Sections of homogeneous, single-phase glasses are also very small, sometimes on the microscale.²³ This makes relating the composition of the archeological glass to its alteration behavior challenging and obtaining enough mass of a single-phase glass to run quantifiable alteration tests nearly impossible. To address these issues, a homogeneous glass based on the composition of Broborg glass was synthesized. The composition represents a mixture of the felsic and mafic rock materials described in Ref. [4]. The interface between the felsic and mafic glass compositions within an archaeological sample from Broborg is shown in Figure 1, and the location of the glass composition selected for this work is shown with yellow markers. The composition is referred to as the “interstitial glass” composition in this work. The full target composition is listed in Table 1, and the EP determined compositions of the archeological glasses are reported in Table 2.

Mixtures of oxide, carbonate, and oxalate precursors were prepared to obtain 500 g of final glass. These mixtures are referred to as the glass “batch.” The target compositions and source materials for the batches are presented in Tables 1 and 2. Table 2 also provides the measured composition of the synthesized glasses. All components were initially combined by manual mixing, followed by mixing in a rotary mixer (Munson) at 1-h increments with intermittent stirring using a spatula until the powder was visibly mixed with no large solid particles (≈ 4 h total). Glass samples were produced by melting batches in alumina crucibles at 1450°C within a controlled atmosphere furnace (Rapidox). The oxidation state of iron was modified by using either $\text{Fe(III)}_2\text{O}_3$ or $\text{Fe(II)}\text{C}_2\text{O}_4 \cdot 2\text{H}_2\text{O}$ (Sigma-Aldrich) precursors, and the melting environment was varied between air, 5% H_2 –95% N_2 , and 80-kPa water vapor (with an N_2 carrier gas) atmospheres. Samples melted in air are denoted as “air,” whereas glass melted in forming gas are denoted with “ H_2 ,” and samples melted in 80 kPa water vapor are denoted with “ H_2O .” The melting process was observed with pressed pellets made of laboratory chemicals in air or water vapor atmospheres. The glass samples were cooled in the furnace to room temperature following melting.

Samples were either cut or powdered for further analyses. The glass powders were prepared by sieving crushed glass between 74 and 149 μm and, subsequently, washed first with deionized water and then with ethanol to remove adhered fines. Glass monoliths were cut using a diamond wafering blade (Kobalt), mounted in epoxy, polished using 400 grit ($\approx 23 \mu\text{m}$), 600 grit ($\approx 16 \mu\text{m}$), 800 grit ($\approx 13 \mu\text{m}$),

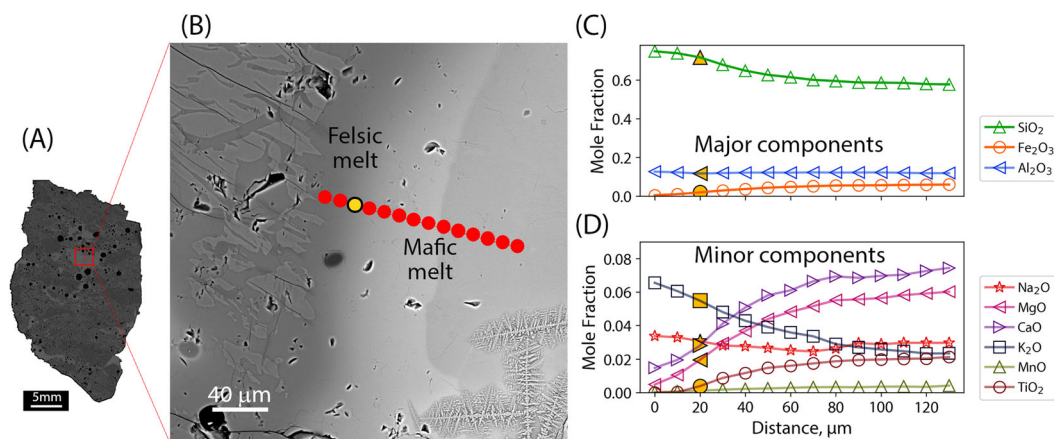


FIGURE 1 (A and B) Archeological sample from the Broborg edifice observed using backscatter electron (BSE) imaging with a scanning electron microscope (SEM) reproduced from McCloy et al.⁴; (C) content of major components measured along the series of red circles indicated in (B) using energy-dispersive spectroscopy (EDS); (D) content of minor components measured along the series of points indicated in (B) using EDS. Plots in (C) and (D) share the same X-axis, and units of mole fraction are defined within the text. The yellow markers in (B)–(D) denote the glass composition that is the focus of this study. The relative analytical uncertainty (1σ) for each compositional measurement is $\pm 5\%$; determined using experimental counting statistics.

TABLE 1 Approximate compositions of glass batches (in g source material per g glass)

Oxide sources for elements	Interstitial glass— Fe_2O_3	Interstitial glass— FeC_2O_4
Al_2O_3 (Alfa Aesar, 99%)	0.175	0.175
CaCO_3 (Noah Chemical, 98%)	0.041	0.041
Fe_2O_3 (J. T. Baker, 98%)	0.046	–
$\text{FeC}_2\text{O}_4 \cdot 2\text{H}_2\text{O}$ (Sigma-Aldrich, 99%)	–	0.103
K_2CO_3 (Fisher Scientific, 99+%)	0.111	0.111
MgO (Fisher Scientific, 95%)	0.016	0.016
MnO (Alfa Aesar, 99.99%)	0.001	0.001
Na_2CO_3 (Fisher Scientific, 98%)	0.048	0.048
SiO_2 (U.S. Silica, 99.5%)	0.634	0.634
TiO_2 (Fisher Scientific, 99.999%)	0.005	0.005
Total	1.078	1.136

and 1200 grit ($\approx 8 \mu\text{m}$) SiC grinding discs (Allied Inc.) then polished with $1\text{-}\mu\text{m}$ diamond polishing suspension (Allied Inc.).

Two other glasses were produced by melting amphibolite rocks (named here the *dike* and *site 5*) obtained from near the Broborg hillfort. The compositions of these rock samples are described in Refs. [30, 36]. A summary of the experiments conducted in this work on one or several of these glasses is given in Table 3.

2.2 | Scanning electron microscopy and electron probe microanalysis

Scanning electron microscopy (SEM) of glass powders was performed using a JEOL JSM 7001F thermal field emission SEM operated with 15-kV accelerating voltage and

20-nA probe current. The powders were mounted on adhesive carbon tape, and imaging was conducted to check for fines.

Bulk compositional analysis of glass monoliths was performed using a JEOL 8530F electron probe microanalyzer operated with 15-kV accelerating voltage, 20-nA probe current, and $20\text{-}\mu\text{m}$ defocused beam. All samples were sputter coated with $\approx 2\text{-nm}$ Ir. For more details on the EPMA measurements, see Table S1.

2.3 | Observation of volumetric batch expansion

VBE measurements were performed to determine the melting behavior of glass batches, especially the onset of foaming which is related to the formation of an early

TABLE 2 Bulk glass compositions in mole percent (mole per 100 moles) and measured uncertainty based on 95% confidence interval determined using experimental counting statistics from $n = 15$ measurements for each glass

Component	Interstitial glass samples				Literature values, amphibolite glasses	
	Measured through EPMA			Target composition	Dike amphibolite glass	Site 5 amphibolite glass
	Glass 1 Fe ₂ O ₃ -H ₂	Glass 2 Fe ₂ O ₃ -air	Glass 3 FeC ₂ O ₄ -air			
Al ₂ O ₃	12.04 ± 0.26	13.15 ± 0.53	11.5 ± 0.31	11.7	9.36	11.21
CaO	2.74 ± 0.04	2.61 ± 0.10	2.99 ± 0.10	2.8	11.41	6.24
Fe ₂ O ₃	1.91 ± 0.02	1.93 ± 0.04	1.91 ± 0.04	1.95	5.38	2.97
K ₂ O	5.08 ± 0.02	5.17 ± 0.03	5.27 ± 0.03	5.48	0.92	1.63
MgO	0.57 ± 0.01	2.24 ± 0.06	4.23 ± 0.07	2.73	11.22	3.31
MnO	0.12 ± 0.01	0.12 ± 0.01	0.11 ± 0.01	0.12	0.28	0.09
Na ₂ O	3.24 ± 0.03	3.23 ± 0.06	3.15 ± 0.05	3.07	3.08	3.11
SiO ₂	73.83 ± 0.24	71.07 ± 0.66	70.44 ± 0.23	71.76	57.46	70.63
TiO ₂	0.47 ± 0.01	0.47 ± 0.02	0.41 ± 0.01	0.38	0.76	0.7
P ₂ O ₅	0	0	0	0	0.1	0.1
ZnO	0	0	0	0	0.02	0
ZrO ₂	0	0	0	0	0.01	0
Sum	100	100	100	100	100	100

Note: Interstitial glass samples were measured through EPMA (described in Section 2.2). Literature values for the dike and site 5 amphibolite glasses, converted from weight percent values listed in Nava-Farias et al.³⁰

Abbreviation: EPMA, electron probe microanalysis.

TABLE 3 Summary table of experimental methods

Measurement	Sample designation					Dike amphibolite glass	Site 5 amphibolite glass
	Fe ₂ O ₃ batch	FeC ₂ O ₄ batch	Fe ₂ O ₃ -H ₂ glass	Fe ₂ O ₃ -air glass	FeC ₂ O ₄ -air glass		
VBE (air or water vapor atmosphere)	X	X					
EGA	X	X					
EPMA bulk compositional analysis			X	X	X		
Static alteration testing			X	X	X		
Room-temperature XANES			X	X	X		
Wet chemical iron redox			X	X	X		
XRD			X	X	X		
Dilatometry			X		X		
High-temperature oxygen probe			X				
High-temperature XANES			X			X	X

Note: The Xs indicate which experiments were performed on the samples in each column.

Abbreviations: EGA, evolved gas analysis; EPMA, electron probe microanalysis; VBE, volumetric batch expansion; XRD, X-ray diffraction.

glass-forming melt. VBE measurements were completed with pressed batch pellets prepared using a 13-mm diameter die and applying 170-MPa pressure to 0.5 g of batch powder. The melting progress was imaged through a viewport into the furnace and as the batched pellets

were heated from room temperature to 1450°C at a rate of 10°C min⁻¹. The melting was observed under dry and water vapor atmospheres. The water vapor atmosphere was induced around the pellet by flowing 50 ml min⁻¹ N₂ gas (99.5% pure) over a water bath heated to 95°C and then

into a silica glass tube located directly above the batch pellets. A large silica glass tube was placed around the reacting pellet to confine the gas flow. A calibrated control thermocouple was placed near the pellet within the silica glass tube to record the furnace's temperature. Further details of this process can be found in Ref. [37].

2.4 | Evolved gas analysis

EGA was performed with 1.0-g batch samples placed in silica tubes within a furnace attached to an Agilent 6890N/5973N gas chromatograph–mass spectrometry system. Batch samples were heated from room temperature to 1450°C at 10°C min⁻¹. He carrier gas (99.999%) was used at a flow rate of 50 ml min⁻¹.

2.5 | High-temperature oxygen partial pressure measurement

High-temperature oxygen partial pressure measurements were carried out using a GS Rapidox II furnace (Glass Service, Czech Republic) using the Fe₂O₃-bearing batch in air. An Ni–NiO sensor (Glass Service, Czech Republic) was immersed into 100 g of molten glass at 1450°C while the sample rotated at 1 rpm. Isothermal holds of 25–30 min were conducted on cooling from 1450°C to temperatures of 1400, 1350, 1300, and 1250°C. Cooling was performed stepwise in 50°C increments. The initial isothermal dwell at 1450°C was performed for ~120 min.

2.6 | X-ray diffraction

X-ray diffraction (XRD) was performed using a PANalytical X'Pert Pro MPD with a Co K_α tube source operated at 40 kV and 40 mA. Glass powders were measured in the range of 5°–90° 2θ with 0.05° step and 10-s dwell time. Five repeated measurements were performed for each sample, and the resulting data was averaged.

2.7 | High-temperature X-ray absorption near-edge structure spectroscopy

High-temperature XANES was performed at the Optique Dispersive EXAFS (ODE) bending magnet beamline of the SOLEIL Synchrotron facility (Saint Aubin, France) operated in top-up mode. Energy-dispersive Fe K-edge XANES was performed in transmission geometry. Incident X-rays were monochromatized using an Si (311) double-crystal apparatus. Spectra were measured in the energy range of 7080–7250 eV with 50–330-ms exposure. X-ray energies

were calibrated to the first inflection point of the Fe K-edge spectra of iron foil at 7112 eV. An amount of ~5–10-mg glass powder was crushed with an agate mortar and pestle and loaded onto a platinum wire following the methods of Mysen and Frantz³⁸ and Neuville et al.,³⁹ and also used by Le Losq et al. and Magnien et al.^{10,40} Isothermal heating trials were conducted between 880 and 1430°C. Cooling was performed cyclically by first heating to a desired melt temperature (between 1050 and 1430°C) then cooling to a desired hold temperature followed by reheating to the initial melt temperature. The heating and cooling rates were not controlled but were ~1°C s⁻¹ considering the small sample size and the direct contact with the platinum heating filament.

The average Fe oxidation states in the glasses were determined by a detailed analysis of the pre-edge peaks. These features relate to the 1s → 3d and/or 1s → 4p electronic transitions.⁸ Data analysis of the pre-edge peak was carried out by subtracting a fitted arctangent background to the normalized absorbance data (to simulate the absorption edge step) and then fitting two ad hoc pseudo-Voigt peaks to the pre-edge features (further details on the pre-edge analysis are reported in Cicconi et al. and references therein).⁴¹ It should be noted that for the interpretation of long-range ordering, different background functions are preferred, such as inclined arctangent, splines, or bi-Lorentzians/Gaussians.⁴² An example of the data fitting used to determine the background is shown in Figure S1, and the peak fitting to the pre-edge features to produce the variograms is shown in Figure S2. The barycenter or center of mass (centroid) energy position of the pre edge peaks was evaluated and plotted against the integrated peak area to create a variogram. The comparison with data from different reference crystalline materials allowed the assessment of the average Fe oxidation state and oxygen coordination numbers (see Figure 2 in Cicconi et al.⁴³).

2.8 | Dilatometric measurements

Dilatometric measurements were performed with a LINSEIS L75 HS 1600C PT dilatometer (Germany) using 20-mm long by 5-mm diameter glass cylinders heated at 10 K min⁻¹ from room temperature to their dilatometric softening points in a He atmosphere (99.999% pure, L/100 L), as previously described by Kolářová et al.⁴⁴

2.9 | Static alteration testing

Static alteration experiments were performed by immersing 1 g of glass particles in 10 ml of ASTM Type-I deionized water within Teflon vessels at 90°C for up to 100 days,

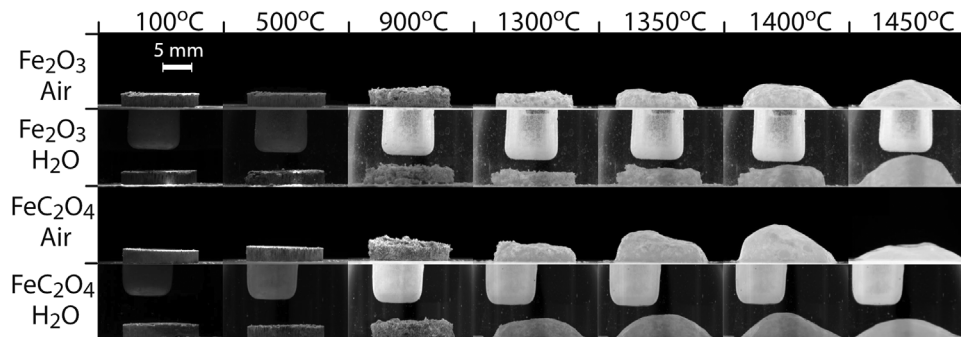


FIGURE 2 Images of batch samples during heating at $10^{\circ}\text{C min}^{-1}$ in either air or water vapor atmospheres. Batch samples were pressed into 13-mm diameter pellets.

similar to the ASTM standard product consistency test method (PCT method B).⁴⁵ Samples of $250\ \mu\text{l}$ of the leachate were extracted from the leaching vessels after 3, 7, 14, 30, 70, and 100 days and acidified with 2.75 ml of 2% mass fraction HNO_3 solution (g/g basis). The acidified leachate samples were analyzed using inductively coupled plasma (ICP) optical emission spectroscopy. The measured releases of Na and Si were converted to a normalized release (NL_i) by the following equation (as described in the ASTM PCT protocol⁴⁵):

$$\text{NL}_i = \frac{C_i}{f_i \times (S/V)} \quad (1)$$

where C_i is the content of element i in solution (g L^{-1}), f_i is the mass fraction of element i in the sample prior to chemical alteration, and S/V is the surface area of glass to volume of solution ratio ($\approx 2000\ \text{m}^{-1}$) as recommended by the ASTM standard PCT method A⁴⁵ and was controlled by particle sieving.

2.10 | Room-temperature XANES and wet chemical analysis

Fe oxidation states were also obtained using the titration method that involves acid digestion of glass powders and ICP atomic emission spectroscopy.⁴⁶ This method provides values of the relative fractions of reduced iron.

For XANES measurements, pellets were prepared by diluting 10 mg of finely ground glass powder in polyethylene glycol (Sigma-Aldrich, 99% purity) and pressing into a 7-mm diameter pellets at 70 MPa. Measurements were performed at the Advanced Photon Source beamline 12-BM-B in fluorescence mode. Scans were performed in top-up mode in the energy range of 6.9–8.0 keV using an Si (111) monochromator.

Using the Fe oxidation state data and the EPMA compositional analysis, the number of NBOs depends on the following equation:

$$\frac{[\text{Al}_2\text{O}_3] + [\text{Fe}_2\text{O}_3]}{\sum [\text{A}_2\text{O}] + [\text{AeO}]} = x \quad (2)$$

where x (in dimensionless units of mol mol^{-1}) can be either $>$ or $<$ 1. In this formula, $[\]$ indicates molar fraction, A_2O indicates alkali oxide, and AeO indicates a valence 2 modifier. The number of NBOs per tetrahedron was determined using the following equation:

$$\left([\text{Al}_2\text{O}_3] + [\text{Fe}_2\text{O}_3] - \sum [\text{A}_2\text{O}] + [\text{AeO}] \right) \frac{n}{T} = \frac{\text{NBO}}{T} \quad (3)$$

where $n = 3$ for $([\text{Al}_2\text{O}_3] + [\text{Fe}_2\text{O}_3]) / \sum([\text{A}_2\text{O}] + [\text{AeO}]) > 1$, otherwise $n = 2$; T is the molar fraction of fourfold-bonded tetrahedral network-forming species assumed to be the charge-balanced Al_2O_3 and Fe_2O_3 as well as SiO_2 and TiO_2 , whereas $\text{Fe}^{2+}-\text{O}-\text{T}$ bonds are treated as NBOs.¹³

3 | RESULTS

3.1 | Glass composition from EPMA

Table 2 provides measured compositions for the three glasses obtained using EPMA. The glass compositions were within 95% t_{critical} uncertainty (based on $n = 15$ measurements for each glass, see Table 2, and assuming a t -distribution with 95% coverage and 14°C of freedom) of the desired composition, except for Al_2O_3 (for the Fe_2O_3 -air sample, glass 2), MgO (for all glasses, especially the Fe_2O_3 - H_2O sample, glass 1 and the FeC_2O_4 -air sample, glass 3), TiO_2 (slightly higher than target for all glasses), and K_2O (slightly lower than target for all glasses). Excess alumina may have been introduced into the Fe_2O_3 -air

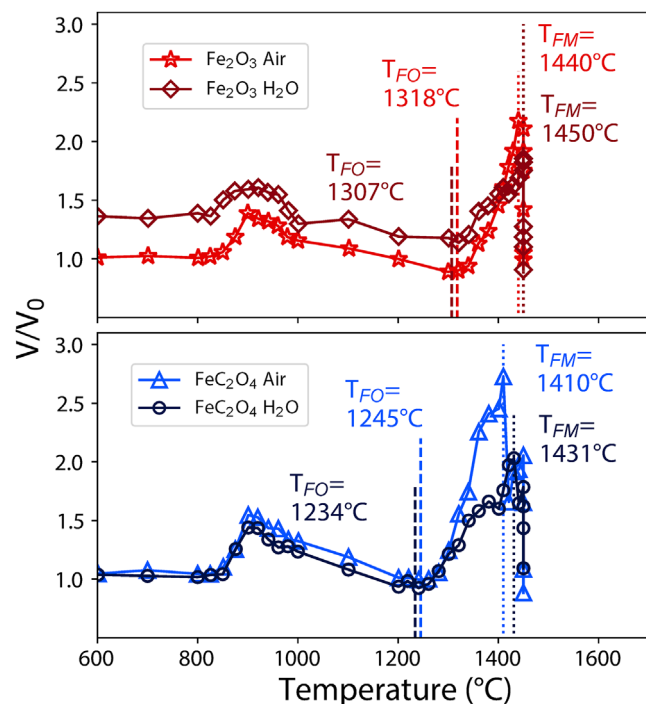


FIGURE 3 Volumetric batch expansion (VBE) of pressed batch pellets during heating at $10^\circ\text{C min}^{-1}$ in air or water vapor atmospheres. The onset of foaming temperatures (T_{FO}) and maximum foaming temperatures (T_{FM}) are shown. The relative analytical uncertainty (1σ) for each expansion measurement is $\pm 5\%$; determined using experimental counting statistics as shown by Marcial et al.³⁷

sample (glass 2) during melting within an alumina crucible (see Sections 2.1 and 2.5). An explanation for the variation among the MgO, TiO₂, and K₂O from the target other than batching error is not available.

Figure S1 provides backscattered electron images of the glass powders used for static alteration tests. Measurements from the images confirm that the particle sizes are within the desired range. Relatively few fine particles were observed on the glass surfaces following the washing step.

3.2 | Influence of Fe oxidation state and water vapor on melting properties

3.2.1 | Pellet VBE

Figure 2 provides images of the VBE measurement during heating of batches in air or water vapor environments. Figure 3 compares the measured volumetric expansion of batches, marking the temperature of foaming onset, T_{FO} , and temperature of maximum foam volume, T_{FM} . Based on Figure 3, the Fe(II)C₂O₄-bearing samples featured $\approx 60^\circ\text{C}$ earlier onset of foaming than the Fe(III)₂O₃-bearing samples. A small expansion was observed near 900°C in

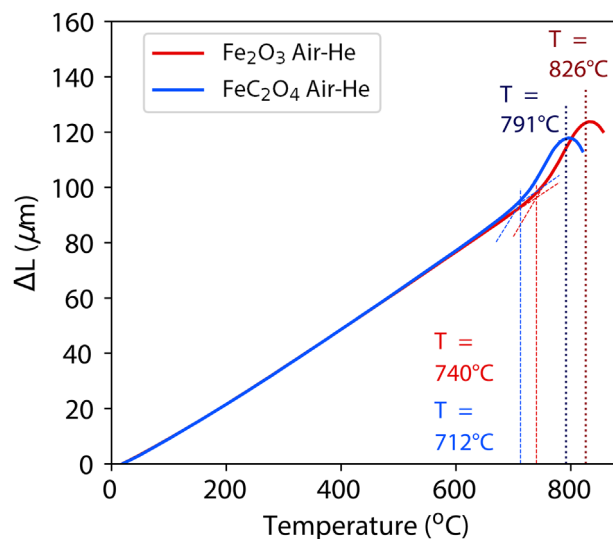


FIGURE 4 Dilatometric measurements of samples during heating at 10 K min^{-1} . The dilatometric transition temperatures (T_g) are the temperatures at the inflection in the dilatometric curve. The dilatometric softening points (T_d) are the temperatures at the curve maxima. The relative analytical uncertainty (1σ) for each expansion measurement is $\pm 2\%$; determined using experimental counting statistics as shown by Kolářová et al.⁴⁴

the four VBE trials and does not significantly change with Fe source or furnace atmosphere. This minor expansion is likely caused by gas escaping from open pores that deform the pellet profile. The EGA results shown in Figure 5, and outlined later, indicate CO₂ gas evolution and support this theory. Figure 2 indicates that the Fe₂O₃-H₂O sample started to lose its initial shape before reaching 900°C . The V/V_0 for this sample between 600 and 800°C is ~ 1.4 (see Figure 3). The expansion in these temperature ranges was the result of oxygen evolution, as will be described in Section 3.3.

3.2.2 | Dilatometry of glass samples

Figure 4 displays the dilatometry results for two glasses during heating in an inert atmosphere. The Fe(II)C₂O₄-bearing sample showed a lower inflection point, which corresponds to the dilatometric transition temperature of the glass (dashed lines in Figure 4), and a lower dilatometric softening point (the maximum of the curve in Figure 4).

3.2.3 | Evolved gas analysis

Figure 5 compares the measured gas evolution during heating of batch powder from room temperature to 1450°C at $10^\circ\text{C min}^{-1}$. During heating, the samples release gas from

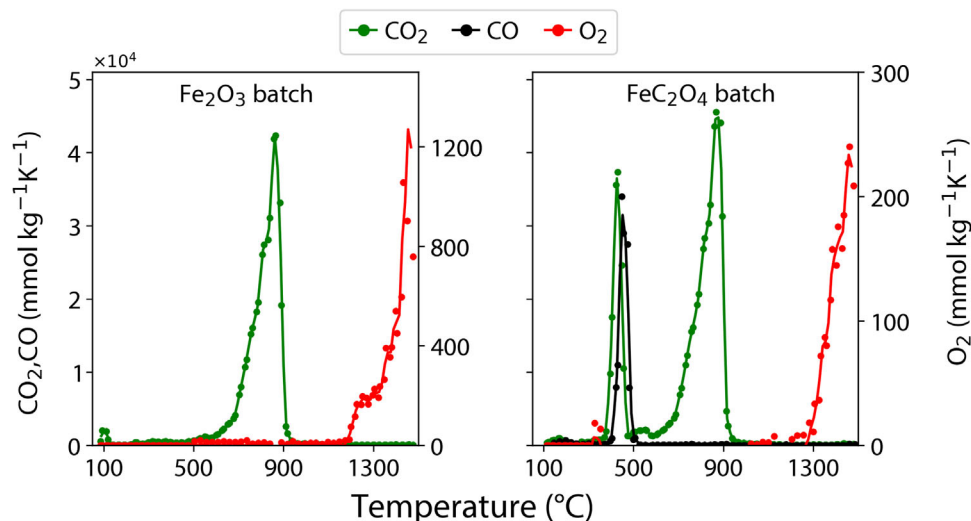


FIGURE 5 Evolved gas analysis of batches heated in helium (He) atmosphere. The relative analytical uncertainty (1σ) for each expansion measurement is $\pm 2\%$; determined using experimental counting statistics as shown by Marcial et al.³⁷ and Hujova et al.⁵⁹

TABLE 4 Compiled values for oxidations state of interstitial glass samples and quarry materials measured on bulk samples at room temperature

Sample	$\text{Fe}^{3+}/\Sigma\text{Fe}$ XANES	NBO/total O	NBO/T	$\text{Fe}^{3+}/\Sigma\text{Fe}$ Wet chemistry	NBO/total O	NBO/T
$\text{Fe}_2\text{O}_3\text{-H}_2$ (quenched from 1425°C)	0.633 ^a	0.002	0.003	0.69	0.006	0.013
$\text{Fe}_2\text{O}_3\text{-air}$ (quenched from 1450°C)	0.575 ^a	0.008	0.015	0.72	0.001	0.03
$\text{FeC}_2\text{O}_4\text{-air}$ (quenched from 1450°C)	0.450 ^a	0.056	0.115	0.55	0.050	0.102
BB dike (heated to 1000°C)	1.000 ^b	0.129	0.278	–	–	–
BB site 5 (heated to 1229°C)	0.925 ^b	0.009	0.017	–	–	–

Note: Table S7 lists the results of this data fitting along with fitting uncertainties.

Abbreviations: NBO, non-bridging oxygen; PEG, polyethylene glycol.

^aMeasured using glass powder mixed into PEG binder.

^bMeasured using in situ XANES measurements of glass melts.

the decomposition of oxalates, carbonates, and hydrated salts in the form of water, carbon dioxide, and carbon monoxide. However, H_2O condenses on the walls of the heating chamber and cannot be reliably quantified; hence, it is omitted from Figure 5. Oxygen is evolved from oxidation–reduction reactions at high temperature in addition to the decomposition reactions.

3.3 | Room-temperature oxidation state

Table 4 provides the calculated values for NBO/total oxygen ($\text{NBO}/\Sigma\text{O}$) and NBO/tetrahedral species (NBO/T) utilizing the measured compositions from Table 2.

Examples of collected profiles can be found in Figure 6. This method provides similar values to an NBO model developed by Vienna et al.⁴⁷; however, that model was developed for complex aluminoborosilicate glasses, and the glass compositions used in this study lie at the extremes for the compositional space of the model. All glasses indicated higher amounts of Fe^{3+} than Fe^{2+} species in their networks. The two melted mineral samples from Broborg showed the highest $\text{Fe}^{3+}/\Sigma\text{Fe}$ values (see Table 4), followed by the $\text{Fe}_2\text{O}_3\text{-air}$ glass, then the $\text{Fe}_2\text{O}_3\text{-H}_2$ glass, and then the $\text{FeC}_2\text{O}_4\text{-air}$ glass. The glass with the highest amount of $\text{NBO}/\Sigma\text{O}$ and NBO/T values was the dike-melted sample, followed by the $\text{FeC}_2\text{O}_4\text{-air}$ glass, then the site 5 and two Fe_2O_3 glasses.

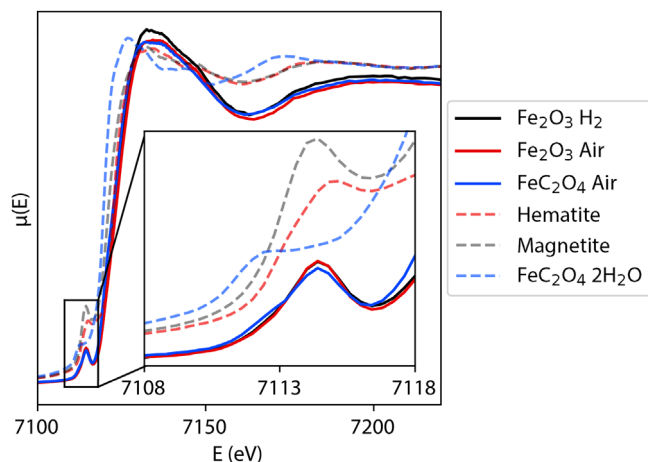


FIGURE 6 Room-temperature X-ray absorption of glass powders. The y-axis is the normalized X-ray absorption as a function of energy, denoted as $\mu(E)$, and is unitless. The inset shows the pre-edge region.

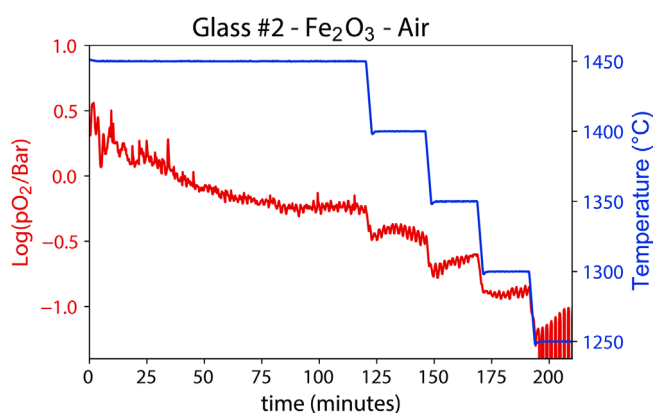


FIGURE 7 Oxygen partial pressure in melt (red) as determined through immersed oxygen probe in melt relative to melt temperature (blue). Stated units are traditional to this measurement with 1 bar = $1\text{E} + 5$ Pa.

3.4 | Oxidation state of Fe—dependence on temperature

Figure 7 displays the measured partial pressure of oxygen in a melt as a function of temperature during cooling for the interstitial glass sample prepared using Fe_2O_3 melted in air. The average oxygen partial pressure decreased upon cooling. Figure 8 compares the variogram and the relative fraction of ferric Fe obtained using high-temperature Fe K-edge XANES of the Fe_2O_3 -air glass to melts produced by heating the two samples obtained from near the Broborg site. Fe reduces at high temperatures for all samples (Figure 8).

3.5 | XRD

Figure 9 compares the measured XRD of the Fe_2O_3 and FeC_2O_4 glasses melted at 1450°C in air or 5% H_2 atmospheres. No strong evidence for crystallization could be observed.

3.6 | Chemical durability

Figure 10 depicts the normalized mass release of Na_2O and SiO_2 as a function of time obtained through static alteration testing of glasses melted under ambient or reducing conditions. The normalized releases of SiO_2 and Na_2O from the three glasses were not found to vary beyond the experimental uncertainty under the conditions tested. The Na release of the Fe_2O_3 - H_2 sample was found to be slightly higher after 30 days had elapsed. Averaged normalized elemental release values and standard deviations are listed in Tables S2–S5.

4 | DISCUSSION

4.1 | Relationship between temperature and oxidation state of the melt

The measured oxidation state of Fe in glass-forming melts as a function of temperature differs from that predicted by models developed by Sack et al.,⁴⁸ Kilinc et al.,⁴⁹ Kress and Carmichael,⁵⁰ and Jayasuriya et al.⁵¹ (Figure 8). These previous studies suggest that $\text{Fe}^{3+}/\sum\text{Fe}$ values are inversely related to changes in temperature. As no crystals were observed in the synthetic glasses (Figure 9), it is unlikely that the formation of crystals during cooling caused this deviation. One hypothesized cause of this observation is the lack of equilibration time provided to the melts. The glasses made in this study were cooled rapidly ($\approx 1^\circ\text{C s}^{-1}$) from $\approx 1050^\circ\text{C}$ (for dike melt) or $\approx 1430^\circ\text{C}$ (for Fe_2O_3 -air glass and site 5 melt) to low temperatures. It is probable that this cooling rate did not provide the Fe within the glass enough time to equilibrate with the surrounding atmosphere. Equilibration is a function of elemental/oxide diffusion rates within melts, and it can be slow when melts have high viscosities.⁵² Interestingly, the measured iron oxidation states for the Fe_2O_3 -air glass as a function of temperature did not match well with the modeled values. One reason for this may be that this glass features a lower fraction of iron than the two amphibolite glasses that are in better agreement with the modeled functions (the synthetic glass contains $\sim 4/100$ g Fe_2O_3 , whereas the other two contain $\sim 12/100$ g Fe_2O_3).

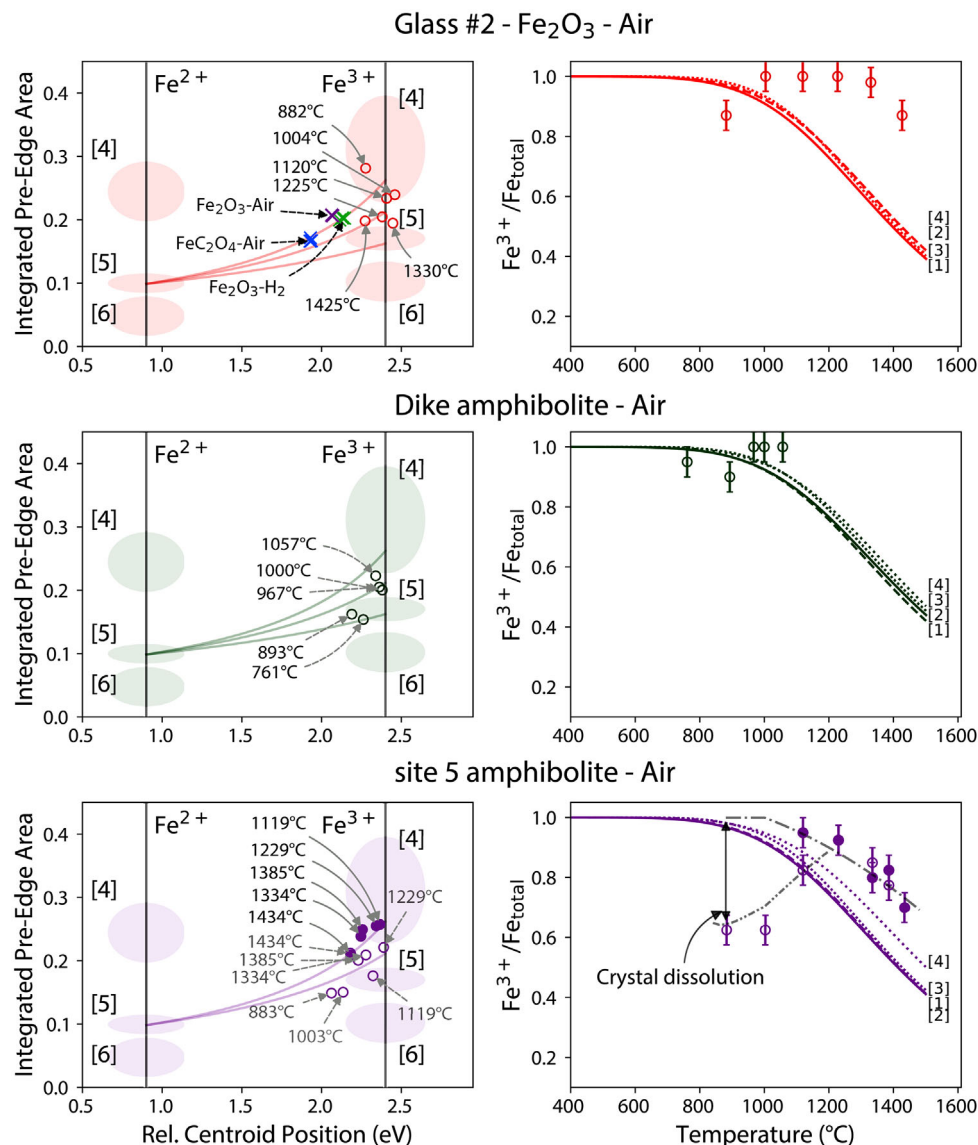


FIGURE 8 Comparison of the iron speciation in interstitial glass prepared with Fe_2O_3 heated in air compared to dike and site 5 amphibolite minerals local to the Broborg hillfort determined using high-temperature XANES. Fe speciation data obtained on cooling from melt is shown as solid points, whereas data obtained on heating of glass powder is shown as hollow points. On the left-hand side, variograms have been prepared to show the variation among the XANES pre-edge features during heating with assumed mixing lines shown for each melt composition. On the right-hand side, calculated values of $\text{Fe}^{3+}/\sum\text{Fe}$ versus temperature (lines) are provided using coefficients obtained from (1) Kilinc et al.,⁴⁹ (2) Jayasuriya et al.,⁵¹ (3) Kress and Carmichael,⁵⁰ and (4) Sack et al.⁴⁸ Labels in the first row are conserved for the plots within their relative column. For the site 5 amphibolite melt, ad hoc lines have been drawn to highlight the variation among the heating and cooling profiles, which is assumed to be caused by crystallization.

In this study, the $\text{Fe}^{3+}/\sum\text{Fe}$ values remain relatively stable for the Fe_2O_3 -air glass until it reaches a temperature between 1150 and 1200°C. This is at the transition between peak CO_2 and O_2 gas production, before the onset of foaming, and after the mass reaches its initial softening point. Near 1200°C, the ratio decreases and remains lower for the remainder of the heating process. This suggests that important redox reactions can occur within these specific melts during their solid-state reaction stage of vitrification. As indicated earlier, further reactions may have occurred if

the melts could equilibrate longer/and or quenched at a slower rate.

The dike sample has a similar, albeit slightly higher redox ratio value as compared to the Fe_2O_3 -air glass. XANES results indicate a redox ratio value decrease for the material around 1050°C, at which time the melting experiment was terminated. The site 5 material had a lower redox ratio value than both the dike and glass sample. This ratio increased as the temperature of the melt increased and as crystals within the material began to

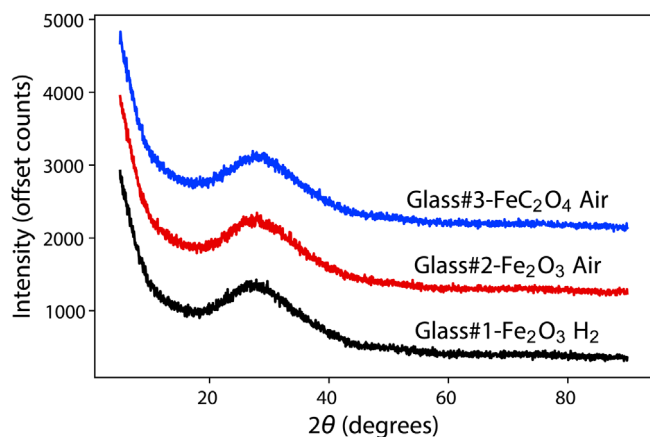


FIGURE 9 X-ray diffraction (XRD) patterns of final glasses. Intensity values (y-axis) are in units of counts.

dissolve into the matrix (see powder sample data for sample in Figure 8). Around 1200°C, this value began to decrease again. This behavior is like that observed for the Fe₂O₃-air glass.

Figure 11 provides the fit of the oxygen partial pressures and compares interpolated values to the oxidation state of Fe determined through high-temperature XANES. There is debate on the local structure of Fe as it reduces from Fe³⁺ to Fe²⁺; however, it appears that Fe²⁺ tends to have a higher average coordination number.^{8,12,40,53–55} The present study supports these findings through the results shown in Figure 11, which is intended to be similar to a Schreiber diagram of $R (=Fe^{3+}/Fe^{2+})$ versus oxygen fugacity.⁵⁶ In the figure (right), the slight negative trend in the R versus $-\log(pO_2)$ graph indicates a higher partial pressure of oxygen in the melt as temperature increases (see also Figure 6). As Fe is the major redox-sensitive species, this trend is likely influenced by the oxygen coordination of Fe. The centroid position and integrated area of the pre-edge peak (Fe variogram, Figure 8) suggest that, at lower temperatures, Fe assumes a tetrahedral coordination, whereas at higher temperature, Fe coordination shifts to higher numbers. However, as mentioned earlier, the lowest temperature value may have been influenced by the rapid quenching schedule and does not follow this trend.

4.2 | Influence of atmosphere on melting behavior

As stated in Section 1, water vapor may have played a role in the melting process of Broborg. However, as indicated in Figure 3, the presence of a water vapor atmosphere did not influence the T_{FO} as significantly as the initial oxidation state of the Fe precursor. The T_{FO} parameter describes

the temperature at which the glass-forming melt connects and closes pores, thereby trapping evolving gases and producing foam.³⁷ In commercial glass batches and nuclear waste feeds, water vapor reduces the surface tension of the glass-forming melt and enhances foaming.³⁷ From VBE experiments, the type of melting atmosphere did not significantly (within the $\pm 5\%$ at 1σ ³⁷) influence the onset of foaming (T_{FO}) or temperature of foaming maximum (T_{FM}) for the Fe₂O₃ or FeC₂O₄ batches. Instead, $\approx 25^\circ\text{C}$ lower T_{FO} was observed among samples prepared with Fe(II)C₂O₄ compared to those prepared with Fe(III)₂O₃ during VBE. The EGA data in Figure 5 demonstrates that the earlier onset of foaming for the Fe(II)C₂O₄-bearing samples in the experiments is not due to a release of gases from the decomposition of oxalate (which produces CO and CO₂) because the EGA for these gases does not coincide with the VBE curves in Figure 3. The foaming for Fe₂O₃ and Fe(II)C₂O₄ batches is due to the evolution of oxygen because of the oxidation–reduction reactions of Fe and, to a minor extent, manganese (Mn).

In Figure 4, the FeC₂O₄-air glass, prepared with an Fe(II) precursor, featured a statistically significant (<2%) lower dilatometric glass transition temperature (T_g) and dilatometric softening point (T_d). However, as seen in Table 2, the fraction of Al₂O₃ and Na₂O in the Fe(II)-based glass is greater than in the Fe₂(III)O₃-air glass. If the NBO/ T calculations were performed for these glasses assuming the same value for Fe(III) as measured for the Fe₂O₃-air glass (0.720), the NBO/ T for the Fe(II)-based glass would be three times greater than for Fe(III)-based glass. This suggests that the T_d of these glass chemistries can be influenced by the degree of melt connectivity, and not strictly by Fe oxidation state.

Evidence that oxidation state did play a role in the melting process of these glasses can be found in the VBE results. These experiments were conducted using pellets of unreacted batch melted under varying atmospheres within a furnace capable of visually observing the conversion from batch to glass on heating. Prior to heating, the Fe oxidation state of the batch is determined by the starting precursor (Fe₂O₃ or FeC₂O₄, see Figure 6 for confirmatory Fe oxidation state measurements), which will evolve over the course of vitrification. According to the XANES results (Table 4), heating of the FeC₂O₄ batch results in a fraction of ferrous Fe undergoing oxidation to reach equilibrium with the oxygen present in the surrounding air environment. The difference observed in T_{FO} (Figure 3) between the Fe(II) (1245°C) and Fe(III) (1318°C) air-quenched glasses is greater than that observed for dilatometric T_g , which are 712 and 740°C, respectively (Figure 4). Therefore, it is likely that the Fe oxidation state was a factor in the reduction of these temperatures, and, by extension, the viscosity of the melt. This observation is

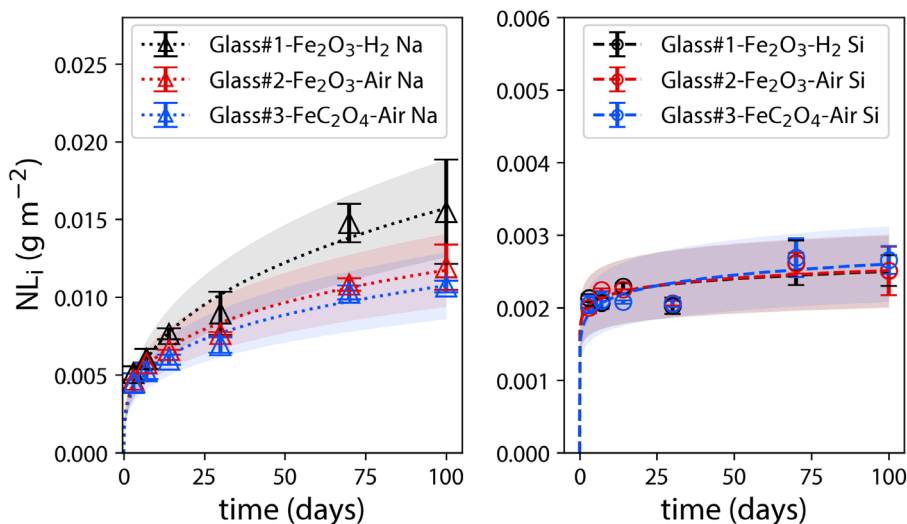


FIGURE 10 Hundred-day static alteration test normalized releases for Na (left) and Si (right) of interstitial glass samples prepared using Fe_2O_3 or FeC_2O_4 melted under different atmospheres. Dotted lines are provided to guide the eye. The 1σ standard deviation, determined using experimental counting statistics of duplicate experiments, is shown using uncertainty bars, and the $\pm 20\%$ experimental uncertainty is shown using a shaded area.

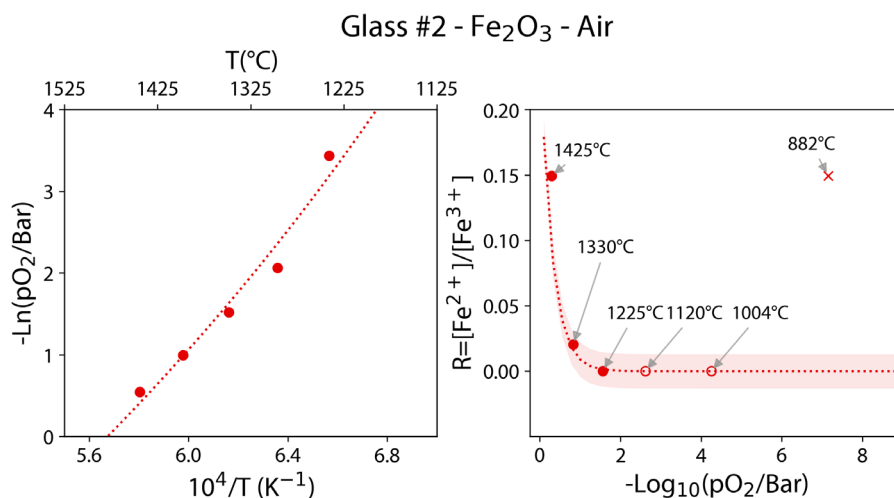


FIGURE 11 (Left) temperature dependence of oxygen partial pressures measured using oxygen probe immersed in melt of glass 2 (see Figure 7), with a linear fit to data shown. (Right) relationship of ferrous-to-ferric iron ratio (determined using high-temperature XANES) to oxygen partial pressure. Closed circles denote that data was collected using both oxygen probe and high-temperature XANES, whereas open circles denote that XANES data was collected, and oxygen partial pressure was calculated using regression equation on left. The shaded area on the right represents a 95% confidence interval for the fit based on the tabulated uncertainties in peak areas listed in Table S7. Non-SI units are defined in the previous figures.

consistent with past research on this topic by Dingwell and Virgo.⁶

4.3 | Influence of non-bridging oxygens on chemical durability

Both composition and Fe redox ratios can influence the release of elements into solution.^{57,58} The normalized fraction of NBOs (NBO/T , Table 4) assumes that Fe

oxidation state influences the degree of network connectivity, which in turn might correlate with the chemical durability (NBO/T is a function of both Fe oxidation state and composition). In this study, it was found that the three synthetic glasses have chemical durability values within experimental uncertainty of one another ($\pm 20\%$ at 1σ , see Figure 10). Of the three, the $Fe_2O_3-H_2$ glass showed the highest Na release. This glass has an Fe redox ratio value between the other two synthesized glass. Therefore, and only for these three glasses, the presence of variable Fe

redox values does not seem to significantly affect glass alteration processes.

5 | CONCLUSION

Two questions were posed to be addressed in this study: (i) did the reducing atmosphere and water vapor from the charcoal fire influence the melting behavior of the raw materials to a significant degree and enhance rock fusion using iron-age technology, and (ii) to what extent did the oxidation state of the melt influence the chemical alteration of the glasses? Regarding the influence on melting properties, it was found that a lower viscosity resulting in a lower glass transition temperature (T_g) softening temperature (T_d) was observed in glasses containing a higher NBO/ T and not necessarily a higher fraction of ferrous iron. A lower temperature of foam onset (T_{FO}) was observed when heating batch containing a ferrous iron precursor suggesting a lower viscosity when the low-temperature glass forming melt is produced. Within glass melts, as the glass melting temperature increases, the redox equilibrium shifts. This equilibrium shift produces ferrous iron that has a greater oxygen coordination than ferric iron. Furthermore, it was found that the effect of the network connectivity had a dominant effect over the effect of a water vapor atmosphere in accelerating the conversion of batch to glass. From these results, it can be proposed that the starting material chemistry may have had a larger influence on how the Broborg glasses melted than the accompanying atmosphere. Regarding the chemical durability of this glass composition, the alteration behavior of three glasses with different degrees of network connectivity was within experimental uncertainty after 100 days of alteration at 90°C in deionized water indicating that the Fe oxidation state for this series of glasses did not influence the alteration behavior. This result suggests that the two glasses found at Broborg may have undergone similar glass alteration rates when considering only alteration by water. Although these glass alteration tests do not exactly mirror the conditions at Broborg over the last 1500 years, they are a valid set of experiments that can be used in adjunct to others and by which to compare observations of analog glass alteration to predicted glass alteration model outcomes.

ACKNOWLEDGMENTS

The authors gratefully acknowledge financial support provided by the Czech Ministry of Education, Youth and Sports (Project No. LTAUSA18075) and by the U.S. Department of Energy (DOE) Waste Treatment and Immobilization Plant Project. Pacific Northwest National Laboratory is operated by Battelle for DOE under contract DE-sAC05-76RL01830. Wet chemical measurements were performed

at ALS laboratories, Prague, CZ. Work included was performed at 12-BM-B beamline of the Advanced Photon Source, by Dr. Sungsik Lee. This research used resources of the Advanced Photon Source, a U.S. Department of Energy (DOE) Office of Science User Facility, operated for the DOE Office of Science by Argonne National Laboratory under Contract No. DE-AC02-06CH11357. Extraordinary facility operations were supported in part by the DOE Office of Science through the National Virtual Biotechnology Laboratory, a consortium of DOE national laboratories focused on the response to COVID-19, with funding provided by the Coronavirus CARES Act. We acknowledge SOLEIL for provision of synchrotron radiation facilities, and we would like to thank Francois Baudalet and Qingyu Kong for assistance in using the ODE beamline. Trade names and commercial products are identified in this paper to specify the experimental procedures in adequate detail. This identification does not imply recommendation or endorsement by the authors or by the National Institute of Standards and Technology, nor does it imply that the products identified are necessarily the best available for the purpose. Contributions of the National Institute of Standards and Technology are not subject to copyright.

ORCID

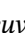
José Marcial  <https://orcid.org/0000-0001-6156-5310>

Richard Pokorný  <https://orcid.org/0000-0002-9023-0381>

John S. McCloy  <https://orcid.org/0000-0001-7476-7771>

Jamie L. Weaver  <https://orcid.org/0000-0002-6762-0568>

Russell J. Hand  <https://orcid.org/0000-0002-5556-5821>

Daniel R. Neuville  <https://orcid.org/0000-0002-8487-5001>

REFERENCES

- Weaver J, McCloy J, Ryan JV, Kruger AA. Ensuring longevity: ancient glasses help predict durability of vitrified nuclear waste. *Am Ceram Soc Bull.* 2016;95(4):18–23.
- Libourel G, Verney-Carron A, Morlok A, Gin S, Sterpenich J, Michelin A, et al. The use of natural and archeological analogues for understanding the long-term behavior of nuclear glasses. *CR Geosci.* 2011;343(2–3):237–45.
- Weaver J, Pearce CI, Sjöblom R, McCloy J, Miller M, Varga T, et al. Pre-Viking Swedish hillfort glass: a prospective long-term alteration analogue for vitrified nuclear waste. *Int J Appl Glass Sci.* 2017;9(4):540–54.
- McCloy JS, Marcial J, Clarke JS, Ahmadzadeh M, Wolff JA, Vicenzi EP, et al. Reproduction of melting behavior for vitrified hillforts based on amphibolite, granite, and basalt lithologies. *Sci Rep.* 2021;11(1):1272.
- Fudali RF. Oxygen fugacities of basaltic and andesitic magmas. *Geochim Cosmochim Acta.* 1965;29:1063–75.
- Dingwell DB, Virgo D. The effect of oxidation state on the viscosity of melts in the system $\text{Na}_2\text{O}-\text{FeO}-\text{Fe}_2\text{O}_3-\text{SiO}_2$. *Geochim Cosmochim Acta.* 1987;51(1):195–205.

7. Mysen B, Richet P. Silicate glasses and melts: properties and structure. Amsterdam: Elsevier; 2005.
8. Wilke M, Farges F, Petit P-E, Brown GE, Martin F. Oxidation state and coordination of Fe in minerals: an Fe K-XANES spectroscopic study. *Am Mineral*. 2001;86(5–6):714–30.
9. Magnien V, Neuville DR, Cormier L, Mysen BO, Briois V, Belin S, et al. Kinetics of iron oxidation in silicate melts: a preliminary XANES study. *Chem Geol*. 2004;213:253–63.
10. Magnien V, Neuville DR, Cormier L, Roux J, Hazemann JL, Pinet O, et al. Kinetics of iron redox reactions in silicate liquids: a high-temperature X-ray absorption and Raman spectroscopy study. *J Nucl Mater*. 2006;352(1–3):190–5.
11. Magnien V, Neuville DR, Cormier L, Roux J, Hazemann J-L, de Ligny D, et al. Kinetics and mechanisms of iron redox reactions in silicate melts: the effects of temperature and alkali cations. *Geochim Cosmochim Acta*. 2008;72:2157–68.
12. Alderman OLG, Lazareva L, Wilding MC, Benmore CJ, Heald SM, Johnson CE, et al. Local structural variation with oxygen fugacity in Fe₂SiO₄ fayalitic iron silicate melts. *Geochim Cosmochim Acta*. 2017;203:15–36.
13. Kim H-I, Sur JC, Lee SK. Effect of iron content on the structure and disorder of iron-bearing sodium silicate glasses: a high-resolution 29 Si and 17 O solid-state NMR study. *Geochim Cosmochim Acta*. 2016;173:160–80.
14. Holland D, Mekki A, Gee IA, McConville CF, Johnson JA, Johnson CE, et al. The structure of sodium iron silicate glass – a multi-technique approach. *J Non-Cryst Solids*. 1999;253(1–3):192–202.
15. Kresten P, Kero L, Chyssler J. Geology of the vitrified hillfort Broborg in Uppland, Sweden. *Geol Fören Stockholm Förh*. 1993;115(1):13–24.
16. Jantzen CM, Plodinec MJ. Thermodynamic model of natural, medieval, and nuclear waste glass durability. *J Non-Cryst Solids*. 1984;67:207–23.
17. Michelin A, Burger E, Leroy E, Foy E, Neff D, Benzerara K, et al. Effect of iron metal and siderite on the durability of simulated archeological glassy material. *Corros Sci*. 2013;76:403–14.
18. Inagaki Y, Ogata A, Furuya H, Idemitsu K, Banba T, Maeda T. Effects of redox condition on waste glass corrosion in the presence of magnetite. *MRS Proc*. 1996;412:257–64.
19. De Echave T, Tribet M, Gin S, Jégou C. Influence of iron on the alteration of the SON68 nuclear glass in the Callovo-Oxfordian groundwater. *Appl Geochem*. 2019;100:268–78.
20. Reiser JT, Parruzot B, Weber MH, Ryan JV, McCloy JS, Wall NA. The use of positrons to survey alteration layers on synthetic nuclear waste glasses. *J Nucl Mater*. 2017;490:75–84.
21. Aréna H, Rébiscoul D, Podor R, Garcès E, Cabie M, Mestre JP, et al. Impact of Fe, Mg and Ca elements on glass alteration: interconnected processes. *Geochim Cosmochim Acta*. 2018;239:420–45.
22. Carriere C, Dillmann P, Gin S, Neff D, Gentaz L, Bruguier F, et al. The fate of Si and Fe while nuclear glass alters with steel and clay. *NPJ Mater Degrad*. 2021;5(1):16.
23. Vicenzi EP, Pearce CI, Weaver JL, McCloy JS, Wight S, Lam T, et al. Compositional imaging and analysis of late iron age glass from the Broborg vitrified hillfort, Sweden. *Microsc Microanal*. 2018;24(S1):2134–5.
24. Gin S, Delaye J-M, Angeli F, Schuller S. Aqueous alteration of silicate glass: state of knowledge and perspectives. *NPJ Mater Degrad*. 2021;5(1):1–20.
25. Thorpe CL, Neeway JJ, Pearce CI, Hand RJ, Fisher AJ, Walling SA, et al. Forty years of durability assessment of nuclear waste glass by standard methods. *NPJ Mater Degrad*. 2021;5(1):61.
26. Frankel GS, Vienna JD, Lian J, Guo X, Gin S, Kim SH, et al. Recent advances in corrosion science applicable to disposal of high-level nuclear waste. *Chem Rev*. 2021;121(20):12327–83.
27. Grambow B. Nuclear waste glasses – how durable? *Elements*. 2006;2(6):357–64.
28. Jantzen CM, Brown KG, Pickett JB. Durable glass for thousands of years. *Int J Appl Glass Sci*. 2010;1(1):38–62.
29. Vienna JD, Ryan JV, Gin S, Inagaki Y. Current understanding and remaining challenges in modeling long-term degradation of borosilicate nuclear waste glasses. *Int J Appl Glass Sci*. 2013;4(4):283–94.
30. Nava-Farias L, Neeway J, Schweiger M, Marcial J, Canfield N, Pearce CI, et al. Applying laboratory methods for durability assessment to archaeological samples: a comparison of laboratory and field results. *NPJ Mater Degrad*. 2021;5(57).
31. Parikh NM. Effect of atmosphere on surface tension of glass. *J Am Ceram Soc*. 1958;41(1):18–22.
32. Dietzel A, Wegner E. Wirkung von Schwefelverbindungen auf die Oberflächenspannung von Emails. *Mitt Ver Dtsch Emailfachl*. 1954;2:13–4.
33. Englund M. Broborg hillfort a research study of the vitrified wall. Stockholm: Arkeologerna; 2018. Contract No.: Report 2018:103.
34. Ahmadzadeh M, García-Lasanta C, Housen B, McCloy JS. Archaeomagnetic dating of vitrified Broborg hillfort in southeast Uppsala, Sweden. *J Archaeol Sci Rep*. 2020;31:102311.
35. Kresten P, Kero L, Chyssler J. Geology of the vitrified hillfort Broborg in Uppland, Sweden. *GFF*. 1993;115(1):13–24.
36. Ogenhall E. Amphibolite rocks near Broborg, Uppland. Report DNR 511-01422-2015. 2016;1(1):1–43.
37. Marcial J, Pokorný R, Kloužek J, Vernerová M, Lee S, Hrma P, et al. Effect of water vapor and thermal history on nuclear waste feed conversion to glass. *Int J Appl Glass Sci*. 2021;12:145–57.
38. Mysen BO, Frantz JD. Raman spectroscopy of silicate melts at magmatic temperatures: Na₂O-SiO₂, K₂O-SiO₂ and Li₂O-SiO₂ binary compositions in the temperature range 25–1475°C. *Chem Geol*. 1992;96(3–4):321–32.
39. Neuville DR, Hennem L, Florian P, de Ligny D. In situ high-temperature experiments. *Rev Mineral Geochem*. 2014;78(1):779–800.
40. Le Losq C, Moretti R, Oppenheimer C, Baudelet F, Neuville DR. In situ XANES study of the influence of varying temperature and oxygen fugacity on iron oxidation state and coordination in a phonolitic melt. *Contrib Mineral Petrol*. 2020;175(7):64.
41. Cicconi MR, Giuli G, Ertel-Ingrisch W, Paris E, Dingwell DB. The effect of the [Na/(Na+K)] ratio on Fe speciation in phonolitic glasses. *Am Mineral*. 2015;100(7):1610–9.
42. Boubnov A, Lichtenberg H, Mangold S, Grunwaldt JD. Identification of the iron oxidation state and coordination geometry in iron oxide- and zeolite-based catalysts using pre-edge XAS analysis. *J Synchrotron Radiat*. 2015;22(2):410–26.
43. Cicconi MR, Le Losq C, Moretti R, Neuville DR. Magmas are the largest repositories and carriers of earth's redox processes. *Elements*. 2020;16(3):173–8.
44. Kolářová M, Kloužková A, Kloužek J, Schwarz J. Thermal behaviour of glazed ceramic bodies. *J Therm Anal Calorim*. 2020;142(1):217–29.

45. ASTM. ASTM C1285-21, standard test methods for determining chemical durability of nuclear, hazardous, and mixed waste glasses and multiphase glass ceramics: the product consistency test (PCT). 2021.
46. Schuessler JA, Botcharkinov RE, Behrens H, Misiti V, Freda C. Amorphous materials: properties, structure, and durability: oxidation state of iron in hydrous phono-tephritic melts. *Am Mineral*. 2008;93(10):1493–504.
47. Vienna JD, Neeway JJ, Ryan JV, Kerisit SN. Impacts of glass composition, pH, and temperature on glass forward dissolution rate. *NPJ Mater Degrad*. 2018;2(1):22.
48. Sack RO, Carmichael ISE, Rivers ML, Ghiorso MS. Ferric-ferrous equilibria in natural silicate liquids at 1 bar. *Contrib Mineral Petrol*. 1980;75:369–76.
49. Kilinc A, Carmichael ISE, Rivers ML, Sack RO. The ferric-ferrous ratio of natural silicate liquids equilibrated in air. *Contrib Mineral Petrol*. 1983;83:136–40.
50. Kress VC, Carmichael ISE. The compressibility of silicate liquids containing Fe₂O₃ and the effect of composition, temperature, oxygen fugacity and pressure on their redox states. *Contrib Mineral Petrol*. 1991;108(1–2):82–92.
51. Jayasuriya KD, O'Neill HSC, Berry AJ, Campbell SJ. A Mössbauer study of the oxidation state of Fe in silicate melts. *Am Mineral*. 2004;89(11–12):1597–609.
52. Schreiber HD. Redox processes in glass-forming melts. *J Non-Cryst Solids*. 1986;84(1–3):129–41.
53. Giuli G, Cicconi MR, Eeckhout SG, Pratesi G, Paris E, Folco L. Australasian microtektites from Antarctica: XAS determination of the Fe oxidation state. *Meteorit Planet Sci*. 2014;49(4):696–705.
54. Fiege A, Ruprecht P, Simon AC, Bell AS, Göttlicher J, Newville M, et al. Calibration of Fe XANES for high-precision determination of Fe oxidation state in glasses: comparison of new and existing results obtained at different synchrotron radiation sources. *Am Mineral*. 2017;102(2):369–80.
55. Nienhuis ET, Tuheen M, Du J, McCloy JS. In situ pair distribution function analysis of crystallizing Fe-silicate melts. *J Mater Sci*. 2021;56(9):5637–57.
56. Schreiber HD, Thanyasiri T, Lauer HV. Redox equilibria of iron in synthetic basaltic melts. *Lunar and Planetary Science Conference Proceedings*. 1979. p. 1070–2.
57. Stranghoener M, Dultz S, Behrens H, Schippers A. Far from equilibrium basaltic glass alteration: the influence of Fe redox state and thermal history on element mobilization. *Geochim Cosmochim Acta*. 2020;273:85–98.
58. Peeler D, Edwards TB. Impact of redox on glass durability: experimental results. WSRC-TR-2004-00313. 2004.
59. Hujova M, Pokorny R, Klouzek J, Lee SM, Traverso JJ, Schweiger MJ, et al. Foaming during nuclear waste melter feeds conversion to glass: application of evolved gas analysis. *Int J Appl Glass Sci*. 2018;9:487–98.

SUPPORTING INFORMATION

Additional supporting information can be found online in the Supporting Information section at the end of this article.

How to cite this article: Marcial J, Cicconi MR, Pearce CI, Klouček J, Neeway JJ, Pokorný R, et al. Effect of network connectivity on behavior of synthetic Broborg hillfort glasses. *J Am Ceram Soc*. 2022;1–16. <https://doi.org/10.1111/jace.18778>